Medical Image Analysis 53 (2019) 132–141

Contents lists available at ScienceDirect

Medical Image Analysis

journal homepage: www.elsevier.com/locate/media

Multiple-correlation similarity for block-matching based fast CT to ultrasound registration in liver interventions☆

Jyotirmoy Banerjee[a], Yuanyuan Sun[a], Camiel Klink[b], Renske Gahrmann[b], Wiro J. Niessen[a,c], Adriaan Moelker[b], Theo van Walsum[a,*]

[a] Biomedical Imaging Group Rotterdam, Departments of Radiology & Nuclear Medicine and Medical Informatics, Erasmus MC – University Medical Center Rotterdam, The Netherlands
[b] Department of Radiology & Nuclear Medicine, Erasmus MC – University Medical Center Rotterdam, The Netherlands
[c] Quantitative Imaging Group, Faculty of Technical Physics, Delft University of Technology, The Netherlands

ARTICLE INFO

Article history:
Received 24 July 2018
Revised 23 January 2019
Accepted 7 February 2019
Available online 7 February 2019

Keywords:
3D
Ultrasound
CT
Liver
Registration
Multimodal

ABSTRACT

In this work we present a fast approach to perform registration of computed tomography to ultrasound volumes for image guided intervention applications. The method is based on a combination of block-matching and outlier rejection. The block-matching uses a correlation based multimodal similarity metric, where the intensity and the gradient of the computed tomography images along with the ultrasound volumes are the input images to find correspondences between blocks in the computed tomography and the ultrasound volumes. A variance and octree based feature point-set selection method is used for selecting distinct and evenly spread point locations for block-matching. Geometric consistency and smoothness criteria are imposed in an outlier rejection step to refine the block-matching results. The block-matching results after outlier rejection are used to determine the affine transformation between the computed tomography and the ultrasound volumes. Various experiments are carried out to assess the optimal performance and the influence of parameters on accuracy and computational time of the registration. A leave-one-patient-out cross-validation registration error of 3.6 mm is achieved over 29 datasets, acquired from 17 patients.

1. Introduction

1.1. Clinical motivation

Computed tomography (CT) is a popular diagnostic imaging technique with high image resolution and, due to fast imaging speed, few motion artifacts. Vessels are not always clearly visible in CT. To image blood vessels, scans are performed after the administration of contrast material. With matrix array probes ultrasound (US) provides real-time 3D imaging. 2D US imaging is used as an intraoperative imaging modality, e.g. in thermal ablation tumor therapy. However, tumors are not always clearly visible in US. Preoperative CT can be combined with 3D US during interventions to incorporate complementary information. Additionally, incorporating CT data during intervention will add greater definition and precision to a US based navigation system.

The purpose of our work is to enable live overlay of CT in US guided tumor ablations. Towards this end we propose a fast registration technique between (preoperative) CT and (intraoperative) 3D US data. Such a method would provide a real-time virtual image overlay of CT on 3D US and thus help the clinicians to accurately visualize the target during the intervention.

1.2. Related work

Several research groups have addressed the registration of CT and US volumes. Lee (2014) used an electromagnetic tracking based fusion imaging of real-time US and CT/Magnetic Resonance (MR) images for percutaneous hepatic intervention of the liver.

Crocetti et al. (2008) performed a feasibility study of CT-US fusion imaging system on ex vivo (calf) livers using a commercially available multimodality fusion imaging system. Recent advances in treatment of liver tumors using image guided ablation techniques are discussed in Kang and Rhim (2015).

There also exist commercial interventional software solutions that perform CT-US registration. These systems typically also use external tracking systems (e.g., electromagnetic, optical) to

☆ **Conflict of interest:** None of the authors has a Conflict of interest to report.

* Corresponding author.
E-mail address: t.vanwalsum@erasmusmc.nl (T. van Walsum).

https://doi.org/10.1016/j.media.2019.02.003
1361-8415/

co-register multimodal images. Optical tracking requires clear line-of-sight between cameras and targets; hence objects inside the body cannot be tracked. Electromagnetic tracking does not require line-of-sight to operate, however these systems are sensitive to ferromagnetic objects. These external tracking based systems provide limited support for soft tissue regions like the abdomen. Some have investigated the potential of using multiple tracked needles for respiratory motion compensation in swines (Zhang et al., 2006), the invasive nature of this approach may limit the applicability in humans.

Registration methods using image information do not suffer from the limitations of active tracking based approaches. Lange et al. (2009) proposed an algorithm that uses intensity and few additional landmark positions to perform non-rigid registration of preoperative CT to intraoperative US volumes. They used the normalized gradient field (NGF) to measure the similarity. To automate the estimation of the initial transformation a graph based edge matching algorithm was proposed by Nam et al. (2012), where the edges were extracted from the segmentation of vessels. Their approach performs registration of US and CT volumes of the liver regardless of the patient or probe motion. However, robust segmentation of vessels in US is a challenging task. Nagpal et al. proposed a combination of intensity and point based registration methods to perform multi-vertebrae CT to US registration of the lumbar spine (Nagpal et al., 2015). They used a spring model to constrain the movement of the individual vertebrae.

Other researchers have tried image based similarity metrics to register US images to CT images. As the physics behind US image formation is different from CT, the choice of the similarity metric for the registration algorithm is non-trivial and critical. Mutual information (MI) is a registration metric that is commonly used in multimodal registration where statistical dependency between the modalities is used (Wells et al., 1996; Pluim et al., 2003).

The correlation-ratio (CR) similarity metric is another multimodal metric that uses the functional relationship (i.e. $\mathrm{E}(y|x) = f(x)$) between the modalities (Roche et al., 1998). To address the spatial intensity inhomogeneity in the US images, Rivaz et al. (2015) used a local estimate of the CR similarity metric using patch based registration approach. A bivariate version of the CR was first introduced by Roche et al. (2001). It assumes a polynomial functional relationship of the form $\mathrm{E}(y|x_1, x_2) = f(x_1, x_2)$, where x_1 is the intensity image and x_2 is the gradient image. The gradient of a CT or MR image is considered to approximately replicate the US imaging as the impedance mismatch at tissue borders results in a bright signature between tissues in the US images. Wein et al. (2008) and Fuerst et al. (2014) assume a linear model of the form $\mathrm{E}(y|x_1, x_2) = a_0 + a_1x_1 + a_2x_2$, where the coefficients of the function (a_0, a_1 and a_2) are estimated locally during the LC^2 similarity metric evaluation (Wein et al., 2008). In MR imaging, there is a less direct relationship between the voxel intensities and tissue characteristics relevant for US imaging. To that end, Kuklisova-Murgasova et al. (2013) pre-segmented MR volumes before converting them into pseudo US volumes, which are further registered to US fetal brain volumes.

Self-similarity based methods exploit neighborhood relationships. These measures are relative and independent of the imaging modality. They are inspired by the success of image denoising methods like non-local means (Buades et al., 2005; 2011a; 2011b). As corresponding regions in different imaging modalities have a similar neighborhood relationship, they share similar self-similarity descriptors/signatures. The descriptors are extracted and compared across modalities using monomodal similarity metrics like sum of squared distances (SSD) or sum of absolute differences (SAD). The modality independent neighborhood descriptor (MIND) was used in Heinrich et al. (2012) for the registration of CT and MR scans. A similar self-similarity based method was later used by Heinrich et al. (2013) to register 3D US and MRI scans for neurosurgery.

1.3. Our contributions

We previously developed a fast and robust approach to 3D US-US registration, combining a block-matching approach with a robust outlier rejection (Banerjee et al., 2015; 2016). In this work, we present a similar strategy, adapted for fast CT-US registration. This work has three main contributions: First, we propose a local variance and octree data structure based evenly spread input feature point selection. Second, we reformulate the earlier presented LC^2 metric (Wein et al., 2008) as *multiple correlation coefficient* (MCC), a correlation based multimodal similarity metric and integrate it in a point-set based registration framework. Third, to improve the block-matching results, we extend our previously presented outlier rejection method based on a geometric consistency (Banerjee et al., 2015) with smoothness criteria.

The remaining of the paper is structured as follows. In Section 2 we discuss the CT and 3D US registration approach. The experiments are described and the results are presented in Section 3. The results are analyzed and discussed in Section 4.

2. Method

The method is intended for continuous registration of CT and US images, and assumes that there already is an (approximate) alignment of the images, either based on manual annotation of some landmarks, or another (semi-)automatic procedure. The method consists of four steps, see Fig. 1. First, we adopt an evenly spread input feature point selection strategy for block-matching. This strategy uses local variance to select distinct point locations and an octree data structure to ensure that the points are evenly spread over the image. Second, we employ a block-matching approach to find point correspondences between the US volumes and the CT volumes using the MCC similarity metric. This block-matching process thus provides a displacement vector for each of the features points. Third, the block-matching is followed by an outlier rejection method which rejects the false point correspondences (incorrect displacement vectors) from the block-matching results. Finally, the displacement vectors of the inliers are then used to estimate the affine transformation using Späth (2004). These steps are similar to the earlier work presented in Banerjee et al. (2015) for the US-US registration. For multimodal CT-US registration, we propose the following three changes to the previous framework. First, unlike naive point selection in Banerjee et al. (2015), we propose a method to select evenly spread feature points. Second, we propose a fast multimodal similarity metric for the multimodal block-matching. Third, the outlier rejection step is adapted and improved over the earlier work presented in Banerjee et al. (2015).

2.1. Selecting input feature point-set for block-matching

The registration method is based on a block-matching strategy (Ourselin et al., 2000; Commowick et al., 2012). Block-matching helps in finding a set of corresponding locations in the reference image $\{p_i\}$ and the moving image $\{q_i\}$, where $1 \leq i \leq n$ and n is the number of elements in the set. A set of input locations for the block-matching is selected from a region of interest (ROI) using the strategy described below. The ROI is the intersection of the liver mask and the (initialized/roughly aligned) US mask, see Fig. 2. Manual segmentation was performed to obtain the liver mask from the CTA volume, but (semi-)automated methods (Heimann et al., 2009) could be applied as well.

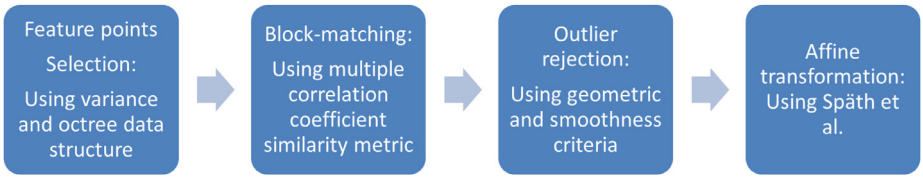

Fig. 1. Fast CT and ultrasound registration framework.

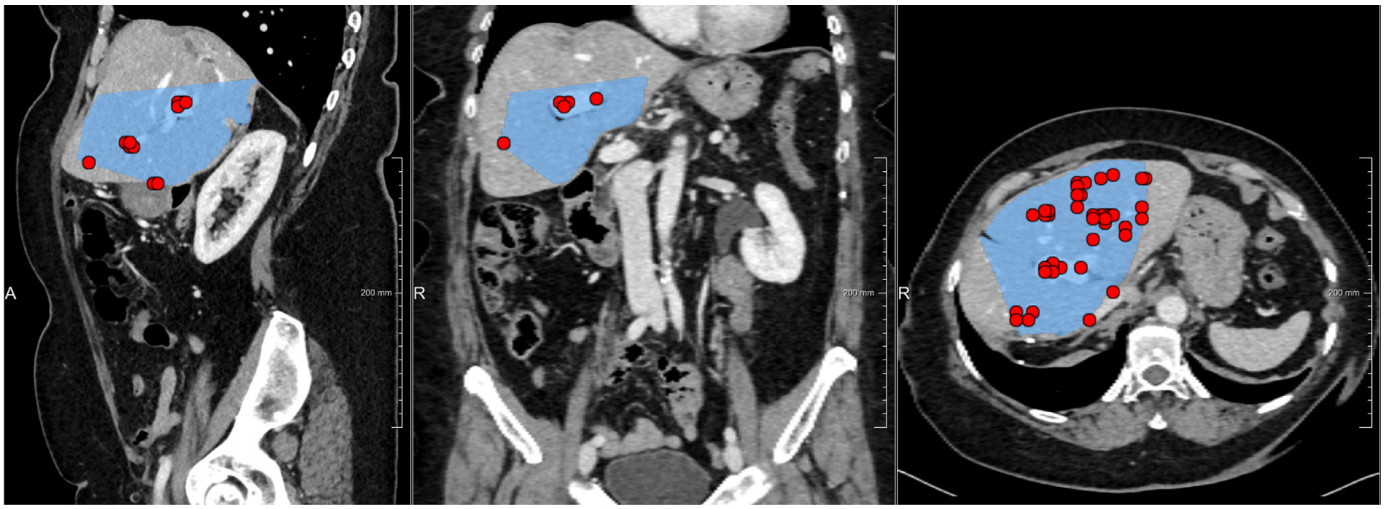

Fig. 2. Feature points selection: Red dots - Variance and octree based feature points selection for block-matching, Blue overlay - Intersection (ROI) of the liver mask and the US mask. (For interpretation of the references to colour in this figure legend, the reader is referred to the web version of this article.)

In this work we adopt an evenly spread feature point selection strategy. We assume that regions in the image with high variance contain information for the registration. Such high variance points in the liver CT image are for example at vessel borders, liver border, or at vessel bifurcations. We employ a strategy that uses local variance to select distinct point locations, and an octree data structure to ensure that the points are evenly spread over the image, see Algorithm 1.

Algorithm 1: Feature points selection.

Data: Input volume
Result: n point locations in the input volume, later used for block-matching
Algorithm:
↪ Select m random point locations in the volume, where $m \gg n$;
↪ Given a block-size of b mm, calculate the variance at the m point locations;
↪ A point location and its corresponding variance value fromthe block, form an octree point;
↪ The m octree points are inserted in an octree datastructure;
↪ Mark all the m octree points as unselected;
while *not n octree points are selected* **do**
  Read an octant, while traversing the octree in a breadth first search fashion;
  for *all the unselected octree points lying inside the octant* **do**
    Select the octree point with the highest variance;
    Mark the octree point as selected;
  end
end

We select m locations from the ROI. Next, n out of m points are selected using an *octree* data structure, where $n \ll m$. To this end, we a block around each of the m points, and we calculate the variance of each of the m blocks. The point and its corresponding variance from the block form an *octree point*. The m *octree points* are inserted in an *octree* data structure. The *octree* partitions the ROI, recursively subdividing it into eight octants. All the m *octree points* are marked as unselected. When selecting the points for the block-matching, the *octree* is traversed in a breadth first search fashion. During this traversal, for each octant, we select the *octree point* with the highest variance, which was not selected earlier. Subsequently, we mark the *octree point* as selected, to ensure that the point is not selected again while traversing the next level of the octree. We continue the breadth first search traversal, until *noctree points* are selected. This approach ensures that the selected n points for the block-matching are points with high variance and evenly spread in the ROI.

2.2. Multimodal block-matching

We use the MCC similarity metric for the multimodal block-matching. MCC finds the correlation between the target variable y and the multiple predictor variables $x_1, x_2, \cdots, x_m$ using a linear model. The square of the coefficient of multiple correlation $\mathcal{R}$ is given by:

$$\mathcal{R}^2 = c^\intercal R_{xx}^{-1} c\,, \tag{1}$$

where

$$R_{xx} = \begin{bmatrix} r_{x_1x_1} & \cdots & r_{x_1x_m} \\ \vdots & \ddots & \vdots \\ r_{x_mx_1} & \cdots & r_{x_mx_m} \end{bmatrix},$$

$c = \begin{bmatrix} r_{x_1y} & \cdots & r_{x_my} \end{bmatrix}^\intercal$ and r_{uv} is the correlation coefficient of the variables u and v.

Similar to Wein et al. (2008) and Fuerst et al. (2014) we assume a linear functional relationship between the CTA intensity volume x_1, the CTA gradient volume x_2 and the US volume y, where $\mathrm{E}(y|x_1, x_2) = a_0 + a_1x_1 + a_2x_2$. However, unlike the regression based method described earlier (Wein et al., 2008; Fuerst et al., 2014) we determine the strength of the association between the variables in an implicit way using a correlation based method. Similar to the normalized correlation coefficient (NCC) an estimate of the coefficients of the linear model is not required to estimate the correlation coefficient in MCC. For MCC with two predictor variables x_1 and x_2, Eq. (1) can be rewritten as:

$$\mathcal{R}^2 = \frac{r_{x_1y}^2 + r_{x_2y}^2 - 2r_{x_1y}r_{x_2y}r_{x_1x_2}}{1 - r_{x_1x_2}^2}\,, \tag{2}$$

where $\mathcal{R} \in [0, 1]$. $\mathcal{R}^2$ is also called coefficient of determination.

The correlation coefficient r_{uv} is calculated using a single-pass approach (Edwards, 1976):

$$r_{uv} = \frac{s\sum u_iv_i - \sum u_i \sum v_i}{\sqrt{s\sum u_i^2 - (\sum u_i)^2}\sqrt{s\sum v_i^2 - (\sum v_i)^2}}\,, \tag{3}$$

where s is the number of samples. Substituting Eq. (3) in Eq. (2), results in a single-pass MCC expression for two predictor variables, which can be efficiently implemented on a graphics processing unit (GPU).

2.3. Outlier rejection

The outlier rejection method is based on the dominant set formulation that we introduced earlier for US-US regsitration (Banerjee et al., 2015). In this approach, an adjacency matrix embedding pairwise constraints, is constructed, and subsequently a homogeneous quadratic term is optimized, yielding the dominant set. Here we first briefly review the geometric constraint that is used to construct the adjacency matrix in the outlier rejection step, originally proposed for the US-US registration (Banerjee et al., 2015). Next, we propose an additional spatio-temporal smoothness constraint to improve the outlier rejection step, which is a prerequisite for a robust CT-US registration. This is followed by a description of the subsequent optimization process.

The outlier rejection method that detects the false correspondences from the previous multimodal block-matching steps is based on the following two criteria:

Geometric criterion: The geometric consistency criterion preserves pairwise distance between locations in the reference image $P = \{p_i\}$ and their corresponding locations in the moving image $Q = \{q_i\}$, where $1 \le i \le n$. The pairwise information is encoded in an adjacency matrix $\mathbf{G}$, where an element of the matrix is given as:

$$G_{i,j} = \begin{cases} e^{-{\delta_{i,j}}^2/2{\sigma_G}^2} & \text{if } i \neq j \\ 0 & \text{otherwise}\,, \end{cases} \tag{4}$$

where

$$\delta_{i,j} = \frac{|\|q_i - q_j\| - \|p_i - p_j\||}{\|q_i - q_j\| + \|p_i - p_j\|}\,.$$

Smoothness criterion: As the geometric consistency criterion does not involve orientation consistency, we added a spatio-temporal smoothness constraint that ensures that the displacement vectors from the block-matching are directionally consistent. Conceptually, this is similar to the piecewise smooth flow field criteria described in the optical flow based method in Brox et al. (2004). However, unlike this optical flow based approach, which tries to find the displacement field between two nearby/consecutive images using a local approach, we address the problem of finding correspondences between two images using a graph-based global approach. The smoothness information is encoded in an adjacency matrix $\mathbf{S}$, where an element of the matrix is given by:

$$S_{i,j} = \begin{cases} e^{-{\zeta_{i,j}}^2/2{\sigma_S}^2} & \text{if } i \neq j \\ 0 & \text{otherwise}\,, \end{cases} \tag{5}$$

where

$$\zeta_{i,j} = \frac{|\overrightarrow{(q_i - p_i)} - \overrightarrow{(q_j - p_j)}|}{\|q_i - q_j\|}\,.$$

Notice that for sufficiently close points q_i and q_j in space, $\zeta_{i,j}$ is the magnitude of the gradient of the flow/deformation vector. Combining the geometric consistency and the smoothness constraint, the optimization function to be maximized is given by:

$$(1 - \eta)\,\mathbf{w}\cdot\mathbf{G}\mathbf{w} + \eta\,\mathbf{w}\cdot\mathbf{S}\mathbf{w}\,, \tag{6}$$

where $0 \le \eta \le 1$ and $\mathbf{w} \in \Delta$. Δ is the unit simplex defined as:

$$\Delta = \{\mathbf{w} \in \mathbb{R}^n : \mathbf{w} \ge \mathbf{0} \text{ and } \mathbf{e}^\intercal\mathbf{w} = 1\}\,, \tag{7}$$

where $\mathbf{e} = [1, \ldots, 1]^\intercal \in \mathbb{R}^n$. The elements of the stochastic vector $\mathbf{w}$ are nonnegative and sum up to one.

The replicator dynamics update equation to maximize Eq. (6) is:

$$w_i(t+1) = w_i(t)\frac{(\mathbf{K}\mathbf{w}(t))_i}{\mathbf{w}(t)\cdot\mathbf{K}\mathbf{w}(t)}\,, \tag{8}$$

where $\mathbf{K} = (1 - \eta)\,\mathbf{G} + \eta\,\mathbf{S}$. The update Eq. (8) ensures that $\forall t$, $\mathbf{w}(t) \in \Delta$ (Weibull, 1995). A local maximum is reached at the location where the trajectory of Eq. (8) does not increase any further (Pavan and Pelillo, 2007). Each element w_i of the vector $\mathbf{w}$ states whether the ith point is an inlier or not. If $w_i < \epsilon$, then w_i is considered as an outlier and the rest of the points are considered as inliers, where ϵ is a small positive real number.

3. Experiments

3.1. Data and resources

3D US was acquired from 17 patients that were scheduled for contrast enhanced CT imaging of the liver. Informed consent was obtained from all patients prior to data acquisition. The clinical motivation for the CT scan was not registered, and the patient imaging data was anonymized before use. 3D US data was acquired using a Philips iU22 US system with an X6-1 probe. For each patient, we tried to get a good ultrasound images from two views: intra-costal (through the ribs), and sub-xiphoidal (below the sternum). The subjects were asked to breath freely during image acquisition. The final data consist of 29 CT-US pairs from 17 patients. The US volume dimensions were 512 × 378 × 222 voxels with voxel size of 0.420 mm × 0.387 mm × 0.629 mm. The contrast-enhanced CT was acquired in the portal venous phase. CT slice thickness was 3 mm, slice spacing was 2 mm except for one case, where slice spacing was 3 mm, and pixel size varied from 0.39 mm × 0.39 mm to 0.75 mm × 0.75 mm.

In addition to this a CT-US pair was acquired on a phantom (Triple Modality 3D Abdominal Phantom, Model 057A). For the phantom, the CT slice thickness was 0.75 mm, slice spacing was 0.4 mm, and pixel size was 0.65 mm × 0.65 mm.

MeVisLab, OpenCL and C++ were used for software development. The OpenCL code was run on a NVIDIA GeForce GTX 1080 Ti GPU.

3.2. Evaluation metric

Manual annotations were performed to obtain ground truth registrations, see Fig. 3. The annotation was challenging, and therefore performed by a clinician with experience in CT and US liver

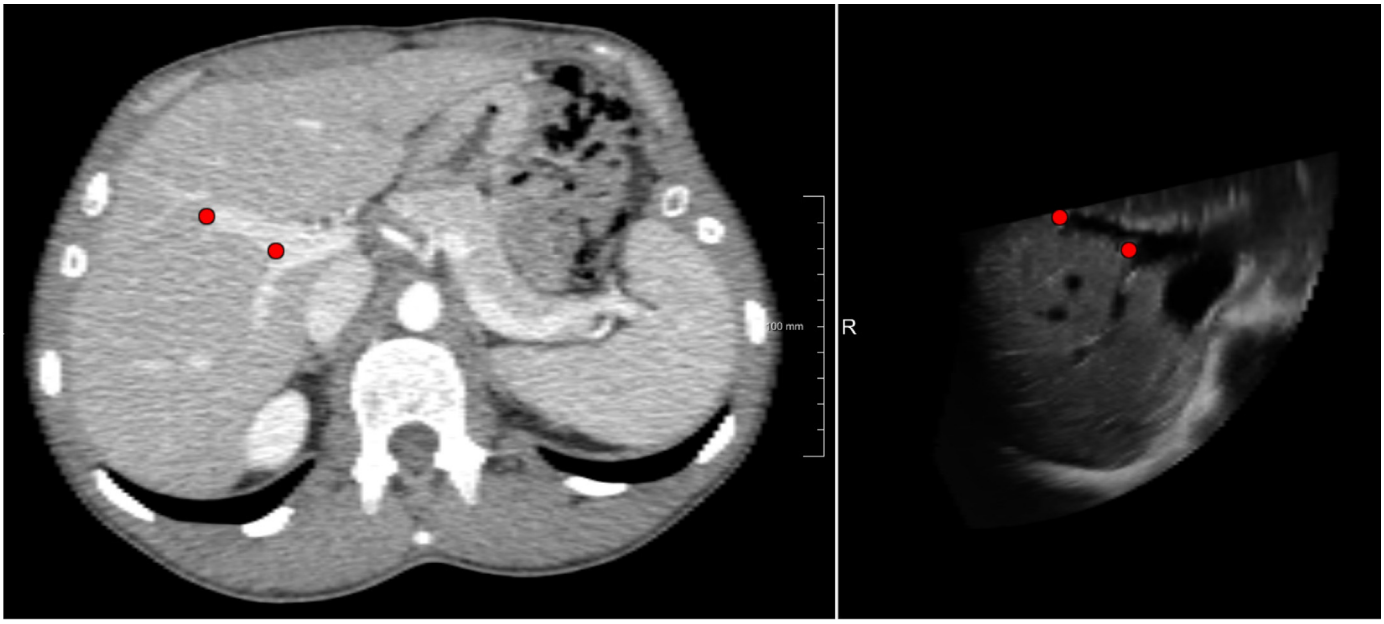

Fig. 3. Sample manual annotations (red dots). (For interpretation of the references to colour in this figure legend, the reader is referred to the web version of this article.)

Table 1
Notations and parameters to optimize in the training experiment.

Symbol	Description
Block-matching -	
n	Number of points
Block-size	Block-size
σ_{CT}	Standard deviation of Gaussian derivative, required to calculate CT gradient
Outlier rejection -	
σ_G	Standard deviation of geometric term
σ_S	Standard deviation of smoothness term
η	Constant in the outlier rejection equation determines the relative weight of the geometric term vs. the smoothness term

imaging. The annotation process was performed in two steps: first a coarse alignment was obtained, after which this alignment was refined by accurately annotating corresponding landmarks. Vessel bifurcations were predominantly used for annotations as these could be uniquely identified in CT and US data. The number of annotations per dataset varied from four to five. The registration error was estimated using the mean target registration error (mTRE (Fitzpatrick and West, 2001)), measured in mm. mTRE is the average distance between the ground truth annotations from the fixed image to the moving image.

3.3. Experiments

We performed the following experiments to tune parameters of the method and to evaluate the performance of the proposed registration method.

- Parameter tuning using leave-one-patient-out cross-validation: We used a leave-one-patient-out cross-validation scheme to assess: the performance and to estimate the optimal parameters of the algorithm, see Table 1. We investigated the effect of change in a) σ_G, b) σ_S, c) η and d) σ_{CT}. We applied a known translation (x, y, z) = (10 mm, 10 mm, 10 mm) (i.e. displacement of 17.3 mm) to the US image which was earlier aligned using the ground truth annotations. The evaluation range of σ_G was {0.1, 0.2, 0.3, 0.4}, of σ_S was {0.25, 0.50, 0.75, 1.00, 1.25}, of η was {0, 0.2, 0.4, 0.6, 0.8, 1} and σ_{CT} was {1 mm, 2 mm, 3 mm}. The number of points and block-size (side length) used in the blocking matching were set to 300 and 15 mm, respectively. The ϵ value was set to 1.19209e−07 (machine epsilon value for the floating type). From the parameter evaluation range we determined the optimal parameter settings based on the mTRE metric.
- Parameter setting sensitivity: To assess the sensitivity of the registration results w.r.t. the optimal parameter settings (using 300 points and 15 mm block size, and a search range of 40 mm), we generated random displacement offsets for x, y and z in the range of [−10, 10] mm. For each image pair we generated five random displacement vectors, thus giving 135 registration results. We then varied the block size (7, 9, 11, 13, 15, 17 mm), number of points for the registration (100, 200, 300, 400, 500) and η (0–1 in steps of 0.1), and plot the mTRE as function of the varying parameter.
- Capture range: The capture range of the method is investigated in a separate experiment. The capture range is likely affected by the search window size: a search window of 20 mm will probably be able to capture displacements in the range [−10, 10] mm. We perform two experiments. First, we use the optimal registration settings with four different search window sizes (5, 10, 20, 40), thereby using the same setup and displacement vectors as in the previous experiment. Additionally, we generated offset vectors using a Gaussian distribution with a σ of 12 mm, 20 per image pair (thus 580 offset vectors) and run the registration with two different search window sizes, 20 and 40 mm, and present the results as scatterplots (initial offset vs mTRE).
- Assessment of point-set selection strategies: Given the optimal parameter setting we studied the performance of the registration approach for a displacement of (10 mm, 10 mm, 10 mm) with respect to the naïve/random point-set selection and compare it to the variance and octree based feature point-set selection on all the 29 CT-US pairs.
- Rotation: In the next experiment we evaluated the robustness of the similarity metric and the block-matching under rotation. We used all the 29 CT-US pairs and aligned them based on

the ground truth annotation. We rotated the US volume in the range from 0 to 30° with a step size of five degrees, where the axis of rotation was $(x = 0, y = 0, z = 1)$, i.e. the default x-y imaging plane of the ultrasound transducer. The CT and the corresponding rotated US volumes were then registered.

- Evaluation on phantom data set: Given the optimal parameter setting we also studied the performance of the registration approach for a displacement of (10 mm, 10 mm, 10 mm) with respect to the ground truth alignment on the phantom data set. Whereas the clinical data assessment reports overall errors (including annotation errors and potential liver deformation), the phantom allows for more accurate annotation and is not subject to respiratory-induced deformations.
- Comparison with other methods: Finally, we ran the method on all data, using an offset of 1, 5 and 10 mm (in x, y and z) from the reference standard, i.e. we applied the offset vector to the US image in its aligned position, and started the registration from there. We compared the registration results with the following methods:
  - Global Mutual Information: Optimizing mutual information over the complete images (using the same liver mask as used for the input point selections);
  - Global LC^2: LC^2 metric as implemented by Carvalho et al. (2014);
  - Local Mutual Information: Optimizing mutual information, where mutual information is computed over local patches;
  - Local LC^2: Optimizing LC^2, where the metric is computed over local patches.

  We used elastix (Klein et al., 2010) as the registration software for the comparison methods. For this method, we used a stochastic gradient decent optimizer, and a multi-resolution registration approach. For the registrations using a global metric, 2048 samples were taken in each iteration. For the local approaches, a volume of $30 \times 30 \times 30$ mm^3 was used for computing the similarity metric in each iteration. This volume size yielded best performance in the pilot experiment.

3.4. Results

The results of the above listed experiments are presented below.

- Parameter tuning using leave-one-patient-out cross-validation: Table 2 shows the registration error per image pair using leave-one-patient-out cross-validation scheme over the 17 patients. Averaging over all the subjects gives a leave-one-patient-out cross-validation registration error of 3.6 (±1.5) mm, when using 300 points and a block size of 15 mm. The registration parameter setting that occured most is σ_G is 0.1, σ_S is 1, η is 0.8 and σ_{CT} is 1 mm, as shown in Table 2. Hence, our optimal parameter setting is 300 points, a block size of 15 mm, σ_G is 0.1, σ_S is 1, η is 0.8 and σ_{CT} is 1 mm. Running this optimal method and averaging the results over all patients gives a mean error of 3.8 (±1.6) mm.
- Parameter setting sensitivity: Figs. 4, 5 and 6 show the mTRE when varying one parameter in the optimal setting chosen in the previous experiment. It demonstrates that for η a value around 0.8–0.9 seems is optimal, and that the registration results degrades slightly if η is chosen larger or smaller. For the blocksize (Fig. 6), the accuracy has converged for a blocksize of 15 mm. Using more points than 300 may still further improve the registration results slightly. However, because the computational times linearly scale with the number of points, we decided to use 300 points in the following experiments. The mTRE for the these settings (with 300 points) over all these registrations is 3.9 (±1.4) mm for affine and 4.2 (±1.5) mm for rigid registration.
- Capture range: Fig. 7 shows the effect of changing the search window size using the same data as in the previous experiment (displacements within [−10, 10] mm). It shows that a search window size that does not match the displacement gives bad registration results (search window 5 or 10 mm). As soon as the search window is sufficiently large to capture the displacement, the registration works fine. This is also shown in the two plots with 580 registration results, with even larger initial

Table 2
Leave-one-patient-out cross-validation rounds. The number of points and block-size are set to 300 and 15 mm, respectively.

Patient	σ_G	σ_S	η	σ_{CT} (in mm)	Error (in mm)
1	0.3	0.5	0.6	1	4.43
2	0.1	1	0.8	1	3.47
3	0.1	1	0.8	1	3.54
4	0.3	0.5	0.8	1	3.52
5	0.1	1	0.8	1	2.70
6	0.3	0.5	0.2	1	3.83
7	0.3	0.5	0.2	1	6.95
8	0.3	0.5	0.8	1	2.14
9	0.3	0.5	0.2	1	3.23
10	0.3	0.5	0.8	1	3.61
11	0.1	1	0.8	1	2.88
12	0.3	0.5	0.2	1	0.34
13	0.3	0.5	0.6	1	5.95
14	0.3	0.5	0.8	1	2.93
15	0.1	1	0.8	1	4.32
16	0.1	1	0.8	1	2.68
17	0.3	0.5	0.8	1	4.45
Average					3.58 (±1.5)

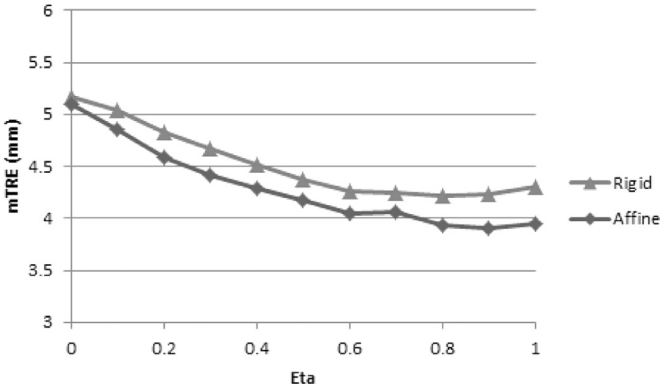

Fig. 4. mTRE as function of η for the optimal settings.

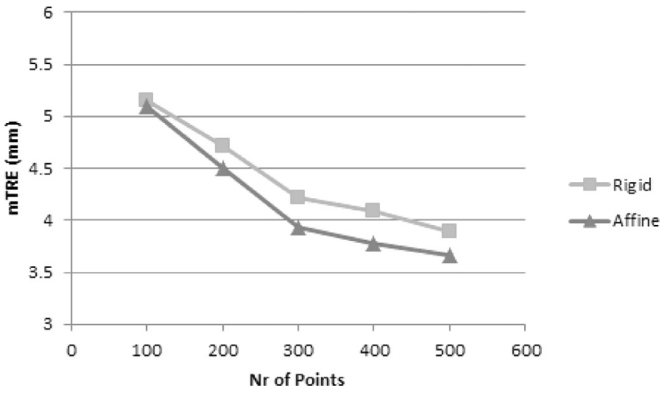

Fig. 5. mTRE as function of number of points for the optimal settings.

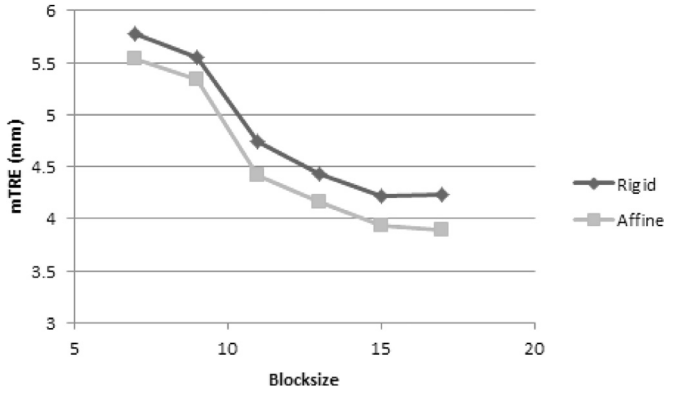

Fig. 6. mTRE as function of blocksize for the optimal settings.

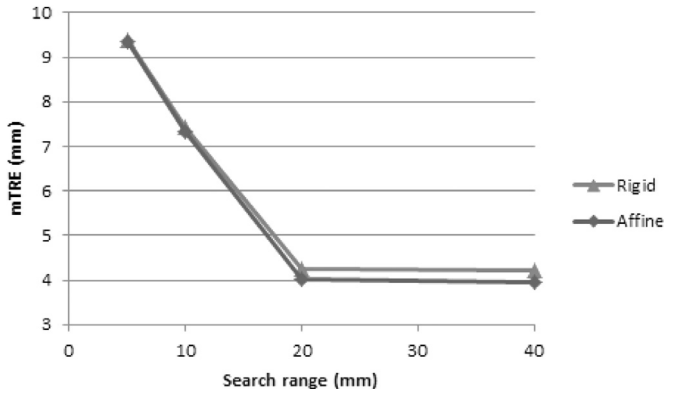

Fig. 7. mTRE as function of search window size for the optimal settings.

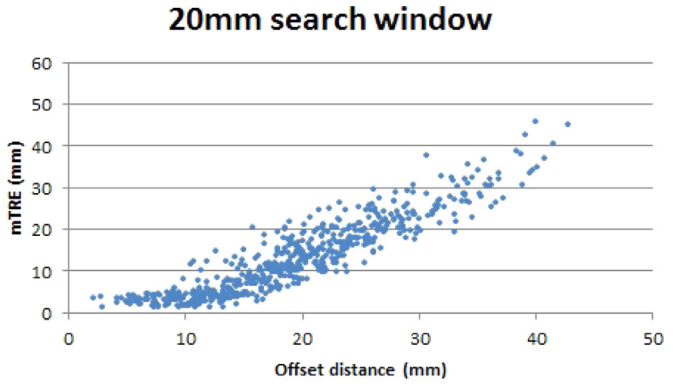

Fig. 8. Capture range plot over 580 registrations, for a search window of 20 mm.

displacements. Fig. 8 shows that a search window of 20 mm is more or less able to correct displacements up to 10 mm, and not beyond, and similarly (Fig. 9) for search widow of 40 mm can register displacements up to 20 mm.

- Assessment of point-set selection strategies: When comparing point selection strategies with the optimal parameter setting, the naive point selection results in 1 mm larger mTRE when 200–400 points are used. This difference is reduced to 0.5 mm for 500 points. The number of levels of the octree structure depends on the number of points required and the shape of the liver mask. For 200 feature points the octree typically has four levels of subdivision.
- Rotation: Fig. 10 shows the results on the rotated dataset. The mTRE value is consistent until 15° of rotation. The registration results deteriorate for rotation angles of 20° or greater.

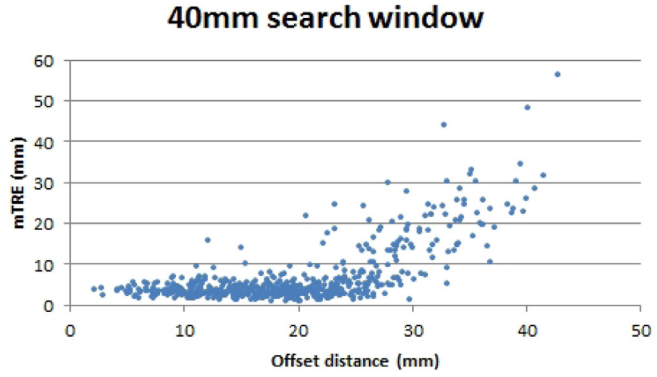

Fig. 9. Capture range plot over 580 registrations, for a search window of 40 mm.

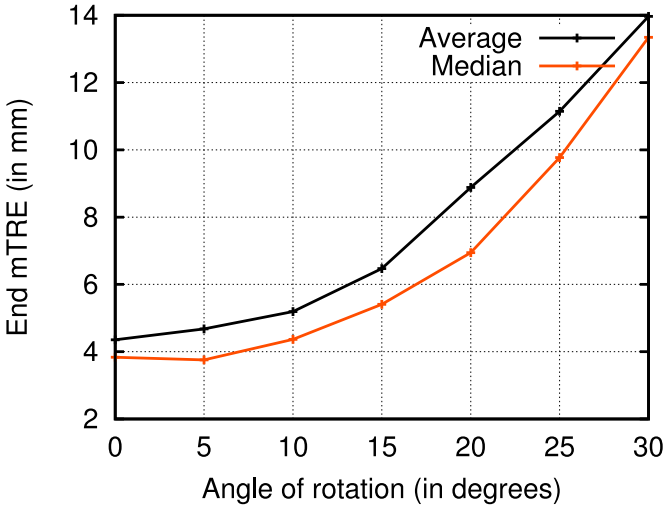

Fig. 10. Registration results on manually rotated US datasets. Block-matching parameters - search grid spacing is 1 mm, block-size is 15 mm, number of points is 300 and σ_{CT} is 1 mm. Outlier rejection parameters - $\sigma_G = 0.1$, $\sigma_S = 1$ and $\eta = 0.8$.

- Evaluation on phantom data set: The registration error using the optimal parameter setting on the phantom data set is 2.1 mm.
- Comparison with other methods: Table 3 gives the results of the comparison with other methods. Global approaches do not work with CT-US registration, as expected. Local variants perform better.

Examples of the registration results are shown in Fig. 13. The GPU timings of the block-matching and the outlier rejection module are shown in Figs. 11 and 12, respectively. For 300 points, block-size of 15 mm and search range of 20 mm the block-matching and outlier rejection modules take 0.27 s and 0.02 s, respectively. Hence the GPU implementation runs the CT and US registration at 3 Hz. Additionally, with 200 points, block-size of 15 mm and search range of 20 mm, for not much decrease in registration accuracy, the block-matching and outlier rejection modules take 0.20 s and 0.01 s, respectively. The GPU implementation would then run the CT and US registration at 5 Hz.

4. Discussion and conclusion

The fusion of pre-operative CT and intra-operative US volumes would provide complementary information from CT during US based image guidance in interventions. In this work we presented a fast CT to 3D US affine registration approach, based on a previously proposed fast 3D US registration framework (Banerjee et al.,

Table 3
Comparison with other methods: mean of landmark error for each of the methods (in mm), and percentage of registration within 5 mm, for three offsets from the ground truth and for rigid and affine registration. BM+OR is block-matching with outlier rejection, MI is mutual information.

Offset	Model	BM+OR	Global MI	Global LC^2	Local MI	Local LC^2
1 mm	rig	4.3 (83)	22 (7)	4.7 (75)	21 (3)	10 (28)
5 mm	rig	4.3 (83)	23 (0)	10 (3)	20 (3)	11 (21)
10 mm	rig	4.1 (79)	27 (0)	19 (0)	28 (0)	17 (3)
1 mm	aff	4.1 (79)	17 (10)	5.6 (48)	17 (3)	7 (41)
5 mm	aff	3.8 (79)	19 (0)	11 (0)	19 (0)	9 (34)
10 mm	aff	3.8 (79)	26 (0)	18 (0)	22 (0)	16 (0)

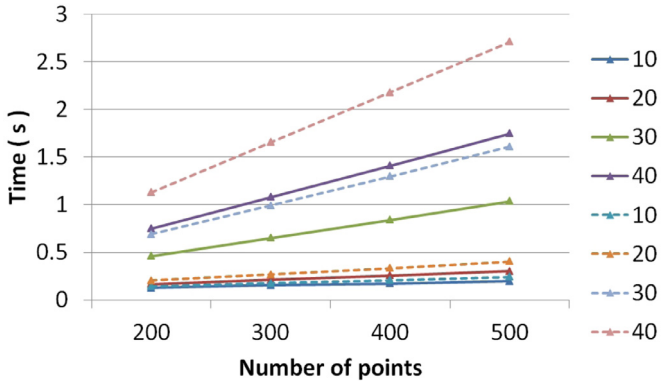

Fig. 11. Block-matching timings. Solid and dotted lines have block-size of 13 mm and 15 mm, respectively. Labels with the lines are search window sizes.

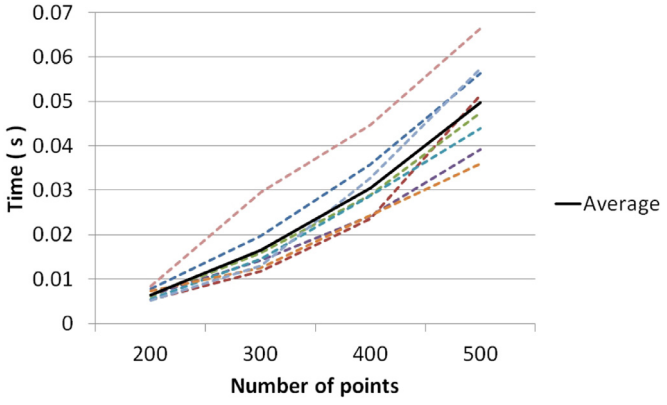

Fig. 12. Outliers rejection timings. The block-matching parameters are set as follows: block-size is 15 mm and search range is 40 mm. Each of the dotted lines represents one dataset.

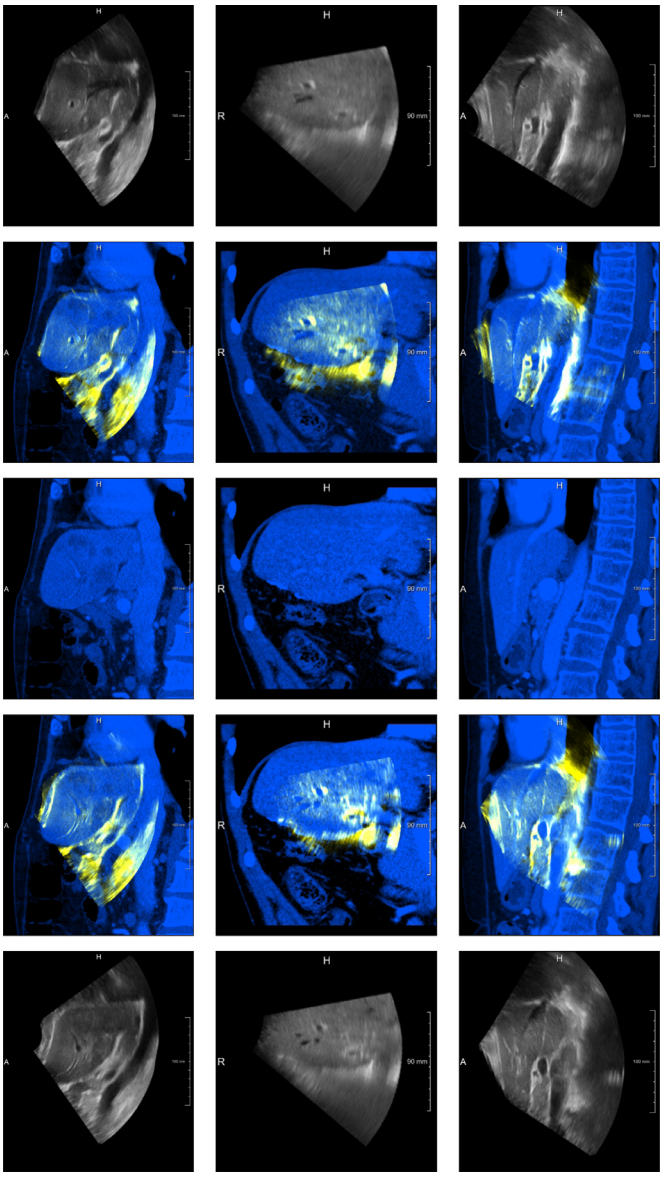

Fig. 13. Registration results for three cases, CT in blue, US in yellow; Top: unregistered ultrasound; 2nd line: unregistered ultrasound with CT; 3rd line: CT; 4th line: registered ultrasound with CT; 5th line: registered ultrasound. (For interpretation of the references to colour in this figure legend, the reader is referred to the web version of this article.)

2015), that enables multimodal registration. The approach consists of four steps namely a) point-set selection, b) block-matching, c) outlier rejection, and d) transformation fitting on the inliers. The block-matching step uses MCC as similarity metric to find correspondences between the CT and the US volumes. We proposed a multimodal similarity metric, which can be efficiently implemented using the GPUs. The block-matching may yield many false correspondences; thus an outlier rejection step was used to remove the false correspondences. We adopt an evenly spread input feature point-set selection strategy using local variance and octree data structure. The main advantage of this feature point-selection strategy is that is allows to get a similar registration accuracy at less computational costs. As the selected points are a locations with structure, it is likely that they are good candidates for the registration. Consequently, the registration method can perform well with less points and a smaller block-size both leading to computational advantages. The method is generic and maybe used in other multimodal registration.

The parameter η weighs between the geometric and smoothness constraint. Fig. 4 shows that the added value of the geometry constraint is marginal; mTRE values at $\eta = 1$ are not much worse

than the mTREs at $\eta = 0.8$). This can be explained by the relation between both metrics: changes in point-pair distances (geometric constraint) may also lead to a smoothness constraint penalty; apparently, the direction consistency is more relevant. Still, the leave-one-out parameter results show that $\eta = 1$ is never part of the optimal set of parameters, suggesting that combining the geometric constraint with the smoothness constraint does have an added value.

Wein et al. (2008) performed affine registration of simulated US from CT and US and achieved a mean registration error of 8.1 mm on 25 liver datasets. They report an average computation time of 28 s (C++ implementation) using the LC^2 similarity measure. The LC^2 similarity measure uses the same linear model as ours $E(y|x_1, x_2) = a_0 + a_1x_1 + a_2x_2$, but unlike our correlation based method it uses a regression based approach to compute the similarity. Though computed differently, the MCC similarity metric and the LC^2 similarity metric are essentially the same under the condition of a linear relationship. Note that the constants (a_0, a_1 and a_2) of the linear model are not explicitly computed for the MCC similarity metric, whereas for LC^2 the coefficients of the linear equation are determined first, after which the metric is computed (Wein et al., 2008). The MCC similarity metric is a function of the pairwise correlation coefficients of all the participating images, the participating images being the CT volume, the gradient of the CT volume and the US volume. Similar to the pairwise correlation coefficient, the MCC similarity metric can be calculated in a single pass. A GPU (NVIDIA GeForce GTX TITAN with 2688 cores) implementation of the LC^2 similarity measure applied to MR and US registration by Fuerst et al. (2014) had an average registration time of 2.32 s for a capture range of 15 mm. The average run-time of our registration method on a GPU (NVIDIA GeForce GTX 1080 with 2560 cores) is approximately 0.2 s for a search range of 20 mm. Lange et al. (2009) performed non-rigid registration on clinical liver data sets of three different patients and achieve a mean registration error of 3.7 mm. Nam et al. (2012) performed affine registration with the joint use of vessels and the liver surface to achieve a fiducial registration error of 3 mm over 20 clinical dataset. Rucker et al. (2014) using sparse surface data performed non-rigid registration of CT and US and achieved a mean registration error of 3.3 mm over 5 phantom deformation dataset. The method we presented has a mean registration error of around 4 mm, which is comparable to other existing registration approaches. In contrast to earlier presented methods, however, the approach presented in this manuscript is able to run in several frames per second, and thus can be used for on-line maintaining the alignment of CT and US images.

The comparison with other methods demonstrates that Mutual Information does not work well with CT-US registrations, which may be caused by variety of appearance in an US image, even for similar tissues. Reduced reflections at more depth, effects of changes in gain settings, shadows because of opaque structures all contribute to this effect, and can generally not be addressed in the acquisition. It is also clear that metrics which model in a more explicit way the relationship between the intensities in both modalities (LC^2, MCC) perform better. For LC^2 we used the implementation available in elastix, which has similar performance for moderate displacements in our data, when comparing to the original work (8.1 mm (Wein et al., 2008)). The main difference between the LC^2 method and the method we propose, next to the computation time, is the additional outlier rejection step, which excludes unreliable point correspondences and focusing on the reliable information. This additional step, which is computationally very cheap, apparently is able to improve the results over integrating the local metric over the complete image.

Other registration methods, such as MIND (Heinrich et al., 2013), were not included in the comparison. Whereas such generic similarity metrics are powerful, the computation of the neighborhood descriptors prior to a registration with multiple values per voxel is likely not matching the computational time requirements for our on-line application.

US and CT fusion guided RFA has shown to be a safe and effective treatment for liver cancer (Xu et al., 2014). In RFA of the liver, interventional radiologist ablates an additional 1 cm thick tumor-free margin around the tumor to avoid reoccurrence of the tumor (Crocetti et al., 2008; McDermott and Gervais, 2013). The registration error of the method presented is in this range. Compared to existing, tracker-based approaches, an image-based fusion approach as presented would logistically be simpler, and would permit automatic updating of the fusion in case of patient motion (such as respiration). For a fast continuous registration of 4D US with CT, the registration to reference by tracking (RTRT) (Banerjee et al., 2016) strategy could be used. The RTRT strategy would help in further reducing the number of points and the search range used in the registration, and would help in improving the run-time of the method. However, real-time 3D US on our system was of inferior image quality (especially the resolution) compared to a static 3D US (3D sweep, obtained in < 1 s using the 2D matrix array transducer). Newer systems may have improved image quality, and permit a live update of the fused images.

Initial US and CT alignment could be done manually, e.g. by locating landmarks (vessel bifurcations) in both modalities. Alternatively, initial alignment using external tracking devices or alignment using an automatic verification strategy (Varnavas et al., 2015; Banerjee et al., 2016), could be employed. Our registration approach is tolerant to rotation up to 10–15 degrees, as shown in Fig. 10. However, there could be large rotation between consecutive US frames due to large probe displacement or change in patient position during complicated surgical procedures. Such motion of the probe or the patient can be accommodated for using an RTRT framework. In our experiments, we consider displacement up to (10 mm, 10 mm, 10 mm), i.e. displacement of 17.3 mm, which is in the range of liver motion. Further, using the RTRT framework proposed in Banerjee et al. (2016), our registration method would require a small search range.

Obtaining accurate CT-US ground truth annotation was a challenging task, especially because the initial orientation of the US data with respect to the CT was not accurately known, as we did not use any external tracking device. To address this we performed annotations in two steps - in the first step we perform rough alignment using an approximate of a few landmark annotations and in the next step we refine the annotation to obtain accurate ground truth annotations. Additionally, we performed the registration on a phantom dataset, where we could obtain accurate ground truth. On the phantom dataset the registration error of 2.1 mm is achieved.

The current approach has been evaluated on data obtained from a single center and a single US device. Validation on a larger test bed should be performed before applying it to clinic. Other avenues of future work include incorporating a respiratory motion model and extension to fast non-rigid registration approaches. Clinical application of the approach will further require to combine it with an effective method to initialize the registration. Conventionally this is done by registering manually annotated landmarks, (semi-)automated approaches for this will also be a direction for future research.

In conclusion, we proposed and evaluated a fast CT to US affine registration which uses a correlation based multimodal similarity metric. The MCC similarity metric expression enables efficient implementation on a GPU. A mTRE of 3.6 mm is achieved over 29 CT and 3D US training pairs acquired from 17 patients. For a search range of 20 mm, the method performs CT and US registration at 5 Hz. The proposed fast CT and US fusion method can be potentially used to improve image guidance in liver interventions.

Acknowledgement

This research is supported by the Dutch Technology Foundation STW, under the STW Project Number 10482 (JB, CK) and a grant 201707720059 of the China Scholarship Council 201707720059 (YS).

References

Banerjee, J., Klink, C., Niessen, W.J., Moelker, A., van Walsum, T., 2016. 4d ultrasound tracking of liver and its verification for TIPS guidance. IEEE Trans. Med. Imaging 35 (1), 52–62. doi:10.1109/TMI.2015.2454056.

Banerjee, J., Klink, C., Peters, E.D., Niessen, W.J., Moelker, A., van Walsum, T., 2015. Fast and robust 3D ultrasound registration - block and game theoretic matching. Med. Image Anal. 20 (1), 173–183. doi:10.1016/j.media.2014.11.004.

Brox, T., Bruhn, A., Papenberg, N., Weickert, J., 2004. High accuracy optical flow estimation based on a theory for warping. In: Computer Vision - ECCV 2004, 8th European Conference on Computer Vision, Prague, Czech Republic, May 11–14, 2004. Proceedings, Part IV, pp. 25–36. doi:10.1007/978-3-540-24673-2_3.

Buades, A., Coll, B., Morel, J., 2005. A non-local algorithm for image denoising. In: 2005 IEEE Computer Society Conference on Computer Vision and Pattern Recognition (CVPR 2005), 20–26 June 2005, San Diego, CA, USA, pp. 60–65. doi:10.1109/CVPR.2005.38.

Buades, A., Coll, B., Morel, J., 2011. Non-local means denoising. IPOL J. 1. doi:10.5201/ipol.2011.bcm_nlm.

Buades, A., Coll, B., Morel, J., 2011. Self-similarity-based image denoising. Commun. ACM 54 (5), 109–117. doi:10.1145/1941487.1941513.

Carvalho, D.D.B., Klein, S., Akkus, Z., van Dijk, A.C., Tang, H., Selwaness, M., Niessen, W.J., 2014. Joint intensity-and-point based registration of free-hand b–mode ultrasound and mri of the carotid artery. Med. Phys. 41 (5).

Commowick, O., Wiest-Daesslé, N., Prima, S., 2012. Block-matching strategies for rigid registration of multimodal medical images. In: ISBI, pp. 700–703.

Crocetti, L., Lencioni, R., Debeni, S., See, T.C., Pina, C.D., Bartolozzi, C., 2008. Targeting liver lesions for radiofrequency ablation: an experimental feasibility study using a ct-us fusion imaging system. Invest. Radiol. 43 (1), 33–39.

Edwards, A.L., 1976. An Introduction to Linear Regression and Correlation. W.H.Freeman & Co Ltd.

Fitzpatrick, J.M., West, J.B., 2001. The distribution of target registration error in rigid-body point-based registration. IEEE Trans. Med. Imaging 20 (9), 917–927. doi:10.1109/42.952729.

Fuerst, B., Wein, W., Müller, M., Navab, N., 2014. Automatic ultrasound-MRI registration for neurosurgery using the 2D and 3D LC^2 metric. Med. Image Anal. 18 (8), 1312–1319. doi:10.1016/j.media.2014.04.008.

Heimann, T., van Ginneken, B., Styner, M., Arzhaeva, Y., Aurich, V., Bauer, C., Beck, A., Becker, C., Beichel, R., Bekes, G., Bello, F., Binnig, G.K., Bischof, H., Bornik, A., Cashman, P., Chi, Y., Cordova, A., Dawant, B.M., Fidrich, M., Furst, J.D., Furukawa, D., Grenacher, L., Hornegger, J., Kainmüller, D., Kitney, R., Kobatake, H., Lamecker, H., Lange, T., Lee, J., Lennon, B., Li, R., Li, S., Meinzer, H., Németh, G., Raicu, D.S., Rau, A., van Rikxoort, E.M., Rousson, M., Ruskó, L., Saddi, K.A., Schmidt, G., Seghers, D., Shimizu, A., Slagmolen, P., Sorantin, E., Soza, G., Susomboon, R., Waite, J.M., Wimmer, A., Wolf, I., 2009. Comparison and evaluation of methods for liver segmentation from CT datasets. IEEE Trans. Med. Imaging 28 (8), 1251–1265. doi:10.1109/TMI.2009.2013851.

Heinrich, M.P., Jenkinson, M., Bhushan, M., Matin, T.N., Gleeson, F., Brady, M., Schnabel, J.A., 2012. MIND: modality independent neighbourhood descriptor for multi-modal deformable registration. Med. Image Anal. 16 (7), 1423–1435. doi:10.1016/j.media.2012.05.008.

Heinrich, M.P., Jenkinson, M., Papiez, B.W., Brady, M., Schnabel, J.A., 2013. Towards realtime multimodal fusion for image-guided interventions using self-similarities. In: Medical Image Computing and Computer-Assisted Intervention - MICCAI 2013 - 16th International Conference, Nagoya, Japan, September 22–26, 2013, Proceedings, Part I, pp. 187–194. doi:10.1007/978-3-642-40811-3_24.

Kang, T.W., Rhim, H., 2015. Recent advances in tumor ablation for hepatocellular carcinoma. Liver Cancer 4 (3), 176–187.

Klein, S., Staring, M., Murphy, K., Viergever, M.A., Pluim, J.P.W., 2010. Elastix: a toolbox for intensity-based medical image registration. IEEE Trans. Med. Imaging 29 (1), 196–205.

Kuklisova-Murgasova, M., Cifor, A., Napolitano, R., Papageorghiou, A., Quaghebeur, G., Rutherford, M.A., Hajnal, J.V., Noble, J.A., Schnabel, J.A., 2013. Registration of 3d fetal neurosonography and MRI. Med. Image Anal. 17 (8), 1137–1150. doi:10.1016/j.media.2013.07.004.

Lange, T., Papenberg, N., Heldmann, S., Modersitzki, J., Fischer, B., Lamecker, H., Schlag, P., 2009. 3D Ultrasound-ct registration of the liver using combined landmark-intensity information. Int. J. Comput. Assist. Radiol. Surg. 4, 79–88. doi: 10.1007/s11548-008-0270-1.

Lee, M.W., 2014. Fusion imaging of real-time ultrasonography with CT or MRI for hepatic intervention. Ultrasonography 33 (4), 227–239.

McDermott, S., Gervais, D.A., 2013. Radiofrequency ablation of liver tumors. Semin. Intervent. Radiol. 30 (1), 49–55. doi:10.1055/s-0033-1333653. 30049[PII].

Nagpal, S., Abolmaesumi, P., Rasoulian, A., Hacihaliloglu, I., Ungi, T., Osborn, J., Lessoway, V.A., Rudan, J., Jaeger, M., Rohling, R.N., Borschneck, D.P., Mousavi, P., 2015. A multi-vertebrae CT to US registration of the lumbar spine in clinical data. Int. J. Comput. Assist. Radiol. Surg. 10 (9), 1371–1381. doi:10.1007/s11548-015-1247-5.

Nam, W.H., Kang, D.-G., Lee, D., Lee, J.Y., Ra, J.B., 2012. Automatic registration between 3D intra-operative ultrasound and pre-operative ct images of the liver based on robust edge matching. Phys. Med. Biol. 57 (1), 69.

Ourselin, S., Roche, A., Prima, S., Ayache, N., 2000. Block matching: a general framework to improve robustness of rigid registration of medical images. In: Medical Image Computing and Computer-Assisted Intervention - MICCAI 2000, Third International Conference, Pittsburgh, Pennsylvania, USA, October 11–14, 2000, Proceedings, pp. 557–566. doi:10.1007/978-3-540-40899-4_57.

Pavan, M., Pelillo, M., 2007. Dominant sets and pairwise clustering. IEEE Trans. Pattern Anal. Mach. Intell. 29 (1), 167–172.

Pluim, J.P.W., Maintz, J.B.A., Viergever, M.A., 2003. Mutual information based registration of medical images: a survey. IEEE Trans. Med. Imaging 22 (8), 986–1004. doi:10.1109/TMI.2003.815867.

Rivaz, H., Chen, S.J., Collins, D.L., 2015. Automatic deformable mr-ultrasound registration for image-guided neurosurgery. IEEE Trans. Med. Imaging 34 (2), 366–380. doi:10.1109/TMI.2014.2354352.

Roche, A., Malandain, G., Pennec, X., Ayache, N., 1998. The correlation ratio as a new similarity measure for multimodal image registration. In: Medical Image Computing and Computer-Assisted Intervention - MICCAI'98, First International Conference, Cambridge, MA, USA, October 11–13, 1998, Proceedings, pp. 1115–1124. doi:10.1007/BFb0056301.

Roche, A., Pennec, X., Malandain, G., Ayache, N., 2001. Rigid registration of 3d ultrasound with MR images: a new approach combining intensity and gradient information. IEEE Trans. Med. Imaging 20 (10), 1038–1049. doi:10.1109/42.959301.

Rucker, D.C., Wu, Y., Clements, L.W., Ondrake, J.E., Pheiffer, T.S., Simpson, A.L., Jarnagin, W.R., Miga, M.I., 2014. A mechanics-based nonrigid registration method for liver surgery using sparse intraoperative data. IEEE Trans. Med. Imaging 33 (1), 147–158. doi:10.1109/TMI.2013.2283016.

Späth, H., 2004. Fitting affine and orthogonal transformations between two sets of points. Math. Commun. 9 (1), 27–34.

Varnavas, A., Carrell, T., Penney, G., 2015. Fully automated 2d–3d registration and verification. Med. Image Anal. 26 (1), 108–119. doi:10.1016/j.media.2015.08.005.

Weibull, J.W., 1995. Evolutionary Game Theory. MIT Press.

Wein, W., Brunke, S., Khamene, A., Callstrom, M.R., Navab, N., 2008. Automatic CT-ultrasound registration for diagnostic imaging and image-guided intervention. Med. Image Anal. 12 (5), 577–585. doi:10.1016/j.media.2008.06.006.

Wells III, W.M., Viola, P.A., Atsumi, H., Nakajima, S., Kikinis, R., 1996. Multi-modal volume registration by maximization of mutual information. Med. Image Anal. 1 (1), 35–51. doi:10.1016/S1361-8415(01)80004-9.

Xu, Z.-F., Xie, X.-Y., Kuang, M., Liu, G.-J., Chen, L.-D., Zheng, Y.-L., Lu, M.-D., 2014. Percutaneous radiofrequency ablation of malignant liver tumors with ultrasound and ct fusion imaging guidance. J. Clin. Ultrasound 42 (6), 321–330. doi:10.1002/jcu.22141.

Zhang, H., Banovac, F., Lin, R., Glossop, N., Wood, B.J., Lindisch, D., Levy, E., Cleary, K., 2006. Electromagnetic tracking for abdominal interventions in computer aided surgery. Comput. Aided Surg. 11 (3), 127–136. doi:10.3109/10929080600751399.